# INVERSION OF SIGNAL PARAMETERS THROUGH SPECTRAL RECOMPOSITION: GEOSCIENCES APPLICATIONS

## Zuniga N. [iD] , Priimenko V.[iD][1]

**Abstract** Analyzing wavelets in the time domain provides an alternative perspective for estimating wavelet parameters and complementing frequency domain analysis. By performing spectral analysis in the time domain with different wavelets, a thorough understanding of their application in diverse geophysical data can be achieved through spectral recomposition-based approaches. Unlike other techniques, our approach does not demand time-frequency transformation.

In this work, we adopt a process that involves reconstructing the spectral content of a signal by calculating its spectrum using a mathematical description and fitting it to an observed spectrum. We implement this approach as an inversion procedure, allowing us to estimate the amplitude, peak frequency, and phase of Gaussian, Semi-Gaussian, and Ricker wavelets across various frequency ranges. Through our implementation and comparisons, we gain valuable insights into the wavelet types that yield optimal results within specific frequency ranges and have shown an efficient manner to estimate wavelet properties in different geophysical methods employed for petroleum exploration.

**Key words:** spectral recomposition, time domain, inversion, wavelet analysis, signal parameters.

**AMS Mathematics Subject Classification:** 86-10, 86A15.

**DOI:** 10.32523/2306-6172-2025-13-1-169-183

## 1 Introduction

Wavelet analysis is a mathematical approach employed in signal processing and data analysis to decompose signals into wavelet functions, capturing localized variations in both time and frequency domains [9]. It enables efficient representation, feature extraction, and denoising of signals, offering valuable insights into complex phenomena across various scientific disciplines [21, 25].

In geosciences, wavelet analysis is crucial in studying seismic data, gravity and magnetic anomalies, petrophysical analysis, electromagnetic waves, and other geophysical signals [19, 26, 27]. Applying wavelet transform techniques can extract valuable information about subsurface structures, geological boundaries, and seismic events [27, 20]. Wavelet analysis facilitates the identification of specific frequency components and their spatial distribution, aiding in the characterization of subsurface features, mapping geological formations, and analyzing seismic wave propagation for an enhanced understanding of subsurface features [20]. Recent works also provided interesting findings regarding improving the signal by incorporating more signal parameters estimation [34, 35], especially in reconstructing the signal [18] and

---
[1]Corresponding Author.

additionally, applying spectral approaches improved signal processing for different geological scenarios [12, 13, 14, 7].

Spectral recomposition is a signal processing technique that involves decomposing a given signal into its constituent frequency components by estimating their amplitudes, frequencies, and phases and then recombining them to reconstruct the modified signal, enabling precise control over its spectral characteristics [28, 17]. Tomasso et al. [32] have developed a mathematical characterization of the Ricker wavelet, which Caio et al. [3] applied as an automatic spectral recomposition approach.

Recent works aimed to apply the spectral recomposition working on a trace-by-trace basis to perform automatic picking of seismic reflections [36], estimate the critical angle and Poisson's ratio in a data-driven manner [37], and optimize starting points for full-waveform inversion ($FWI$) [38]. All these techniques were effective even in random noise with a signal-to-noise ratio ($SNR$) of 2. These works showed that performing an inversion procedure to estimate signal parameters of a Ricker wavelet for seismic data is very enriching. However, they have yet to be committed to analyzing other types of wavelets, which would allow a deeper understanding of the application of spectral recomposition approaches for other geophysical methods.

The approaches mentioned do not require relatively long offsets [16] or transforming the data to other domains, such as the $\tau - p$ domain, see, e.g., [29]. Data in other domains (e.g., $\tau - p$ domain) are often affected by transform artifacts and require other techniques to reduce/suppress these artifacts [5]. Methods for estimating the fundamental properties of a signal can be based on Prony decomposition, which allows for the calculation of the attenuation coefficient in addition to frequency, amplitude, and phase; see [22, 23, 24, 6].

Analyzing wavelets in the time domain and the frequency spectra in the frequency domain allows for estimating wavelet parameters through other perspectives than exploring the frequency spectrum. Since, in the field data analysis, we have to deal with significant noise, performing the estimate of signal parameters in the frequency domain is very efficient for obtaining frequency and amplitude information; however, it also shows some difficulties in estimating the phase and, therefore, the position of a wavelet in time [37, 38]. For this reason, it is interesting to perform this inversion procedure in the time domain and for different wavelets (Gaussian, Semi-Gaussian, and Ricker), which are the most commonly used wavelets for geophysical and petrophysical methods. Employing this approach for other wavelets and frequency ranges allows us to profoundly comprehend the use of these techniques in other geophysical methods, such as $GPR$ (ground penetrating radar) and other electromagnetic methods, or for heat wavefronts and radioactive signals.

In summary, spectral recomposition is indeed a powerful tool in seismic data analysis with multiple applications:

- **enhanced stratigraphic resolution:** it can improve the resolution of stratigraphic features, helping geologists better understand the layering and distribution of rock types;
- **fault detection and analysis:** by focusing on specific frequency ranges, geologists can more clearly delineate fault zones;
- **hydrocarbon detection:** certain frequency bands can indicate the presence of hydrocarbons;
- **seismic inversion:** it assists in seismic inversion processes by providing detailed frequency-based information.
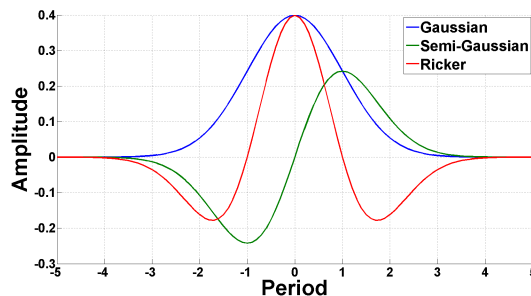- **reservoir characterization:** it helps understand reservoir properties and heterogeneities.

Figure 1: Gaussian, Semi-Gaussian, and Ricker wavelets

In this work, we propose to implement an inversion procedure based on the spectral recomposition approach to reconstruct the spectrum of a signal by fitting the calculated spectrum to an observed one, where the calculated curve is the mathematical representation of each one of the types of wavelets used here (Gaussian, Semi-Gaussian, and Ricker wavelets). This allows us to estimate amplitude, peak frequency, and phase for different frequency ranges ($5\,Hz$, $15\,Hz$, $30\,Hz$, $100\,MHz$, and $1\,GHz$) in noise-free and noisy data. Our implementation allows us to identify which frequency range works best with each wavelet type when estimating their signal parameters in the time domain.

## 2   Ricker, Semi-Gaussian, and Gaussian wavelets

Ricker, Semi-Gaussian, and Gaussian wavelets are different wave functions commonly used in signal processing and geophysical data analysis [10]. The Ricker wavelet, also known as the Mexican hat wavelet, is characterized by its symmetric, bell-shaped waveform. It is widely employed in seismic exploration as it closely resembles the shape of seismic pulses. Seismic source signals generally have a phase that approaches zero. This phase usually shifts as it approaches the critical angle [33].

On the other hand, the semi-Gaussian wavelet is a modified version of the Gaussian wavelet. It possesses a smoother, more Gaussian-like shape with reduced oscillations. This wavelet is often used in applications where a smoother signal representation is desired. The $GPR$ signal, for instance, presents a smooth signal and phase different than zero [15].

The Gaussian wavelet, derived from the Gaussian function, is widely used due to its mathematical simplicity. It has a symmetric shape and offers good localization in both time and frequency domains. Gaussian wavelets are commonly employed in various fields, including image processing, feature extraction, and noise reduction. A Gaussian function can describe the front of a heat flow.

Each wavelet exhibits different characteristics and is selected based on the specific requirements of the analysis or processing task. These characteristics are also related to the difference in how they shift and how sensitive each of these functions is in shifting their phases [10].

The Ricker wavelet [28] can be described, in the time domain, as

$$\psi(t) = \frac{2}{\sqrt{3}\sigma\pi^{1/4}} \left(1 - \frac{t^2}{\sigma^2}\right) \exp\left\{-\frac{t^2}{2\sigma^2}\right\}, \tag{1}$$

where $t$ is the wavelength and $\sigma$ is the dominant wavelength.

In many cases, where the Ricker wavelet of a seismic signal reaches the critical angle, its phase gradually shifts between 0° and 180° as long as it gets close to the critical angle. Another condition where we can observe a 180°-shifted wavelet compared to the Ricker wavelet is in ground-penetrating radar ($GPR$) and other electromagnetic signals.

172 Zuniga N., Priimenko V.

For both cases, we can describe the Semi-Gaussian wavelet as the first derivative of Ricker wavelet [33]:

$$\psi(t) = \frac{2t}{\sqrt{3}\sigma\pi^{1/4}} \exp\left\{-\frac{t^2}{2\sigma^2}\right\}, \tag{2}$$

as the modulus of the derivative in Eq. (1) with respect to $t$ is applied.

Applying the modulus of the derivative to Eq. (2) results in the Gaussian function,

$$\psi(t) = \frac{2\sqrt{\sigma^3}}{\sqrt{3}\pi^{1/4}} \exp\left\{-\frac{t^2}{2\sigma^2}\right\}. \tag{3}$$

Figure 1 shows the three wavelet functions: Ricker, Semi-Gaussian, and Gaussian.

## 3 Method
### 3.1 Spectral Recomposition

Tomasso et al. [32] proposed that the amplitude and phase spectrum of a seismic trace can be expressed as a combination of amplitude and phase spectra of various Ricker wavelets

$$d(f) \approx \sum_{i=1}^{n} a_i\psi_i(m_i, f), \tag{4}$$

where $d(f)$ represents the amplitude and phase spectrum of a seismic trace, $f$ is the frequency, and $a_i$ and $m_i$ represent, respectively, the amplitude and peak frequency of the $i$-th Ricker wavelet spectrum component having the following expression

$$R_i(f) = a_i\psi(m_i, f) = a_i\frac{f^2}{m_i^2} \exp\left\{-\frac{f^2}{m_i^2}\right\}. \tag{5}$$

The spectral recomposition approach can estimate peak frequency and amplitude from a spectrum through its reconstruction, unlike other methods based on spectrum decomposition; see, e.g., [11].

The mathematical description provided by Eqs. (4) and (5) allows us to treat the problem as an inversion. In this approach, we can fit a calculated spectrum to the observed one to obtain estimates of the signal properties of the analyzed wavelet [37, 38]. As Equation (5) was initially developed to characterize the spectrum in the frequency domain, we can apply the objective function to the time domain.

The selected frequencies for being tested in this work cover a range of important methods that can have their utilization represented by these frequency ranges in geosciences. Lower frequencies ($5\,Hz$, $15\,Hz$, and $30\,Hz$) are commonly used in seismic methods, such as for velocity analysis in reflection seismic or $FWI$; frequencies in the order of $100\,MHz$ are commonly used for diverse petrophysics applications; while higher frequencies (around $1\,GHz$) are used for $GPR$.

### 3.2 Objective Function

The model we are working on here is a linear combination of Ricker wavelet spectra. Each spectrum is a nonlinear function dependent on signal parameters. We need the coefficients $a$ (amplitude) and $m$ (peak frequency) to estimate the Ricker wavelet spectra. Then, we can calculate the error using

$$r_j = d(f_j) - \sum_{i=1}^{n} a_i(m_i)\psi(m_i, f_j).$$

The objective function is then formulated as a least-squares estimation

$$\min_{\mathbf{a},\mathbf{m}} \|\mathbf{r}(\mathbf{a}, \mathbf{m})\|_2^2, \tag{6}$$

where $\mathbf{a} = (a_1, \ldots, a_n)$, $\mathbf{m} = (m_1, \ldots, m_n)$, and $\mathbf{r}$ is a vector composed of $r_j$ elements.

However, in the time domain, Eq. (6) can be written as

$$\min_{\mathbf{a}, \boldsymbol{\sigma}} \|\mathbf{r}(\mathbf{a}, \boldsymbol{\sigma})\|_2^2,$$

to consider the signal parameters in the time domain, i.e., using the dominant wavelength $\boldsymbol{\sigma}$ instead of the peak frequency $\mathbf{m}$. This gives us

$$r_j = d(t_j) - \sum_{i=1}^{n} a_i(\sigma_i) \psi(\sigma_i, t_j). \tag{7}$$

By applying Eq. (7) to Eqs. (1)-(3), we obtain the residual error in the time domain for the Ricker wavelet

$$r_j = d(t_j) - \sum_{i=1}^{n} a_i(\sigma_i) \frac{2}{\sqrt{3}\sigma_i \pi^{1/4}} \left( 1 - \frac{t_j^2}{\sigma_i^2} \right) \exp \left\{ -\frac{t_j^2}{2\sigma_i^2} \right\}, \tag{8}$$

and the Semi-Gaussian wavelet,

$$r_j = d(t_j) - \sum_{i=1}^{n} a_i(\sigma_i) \frac{2t_j}{\sqrt{3}\sigma_i \pi^{1/4}} \exp \left\{ -\frac{t_j^2}{2\sigma_i^2} \right\}, \tag{9}$$

and for the Gaussian wavelet

$$r_j = d(t_j) - \sum_{i=1}^{n} a_i(\sigma_i) \frac{2\sqrt{\sigma_i^3}}{\sqrt{3}\pi^{1/4}} \exp \left\{ -\frac{t_j^2}{2\sigma_i^2} \right\}, \tag{10}$$

respectively. This allows us to recover the critical components from the spectrum and analyze the residual error of each wavelet.

Instead of employing global search optimization algorithms, we can combine a local search optimization algorithm with the multi-start procedure, as described by [30]. This routine applies a local search starting from a random initial point $n$ times, which leads to a statistical distribution dependent on the number of iterations. We, then, perform the least-squares minimization between the calculated wavelet spectrum in time, i.e., Eqs. (8)–(10), and the observed wavelet. Each iteration has, as a result, a different minimum value since we are considering a stochastic process, which allows the comparison among the minima of each iteration. Then, we can select the lowest value among the minima. The number of iterations to be set depends on the complexity of the objective function of an analyzed spectrum.

The multi-start procedure can be divided into two steps. The first step involves the sequential trust region algorithm (Fig. 2), which aims to force convergence to a local minimum region starting from a distant initial point of a matrix of variables $\mathbf{X}$. The computed optima do not need to satisfy integrality conditions, which allows for the improvement of local optima.

Terlaky & Sotirov [30] conducted tests on the input parameters ($r_1$, $r_2$, $c_1$, and $c_2$), and we adopted their proposed parameter values for our use. They also assume that the given matrix $\mathbf{B}$ does not need to be positive. Thus, the gradient ascent approach makes the sequential trust region return a matrix $\bar{\mathbf{X}}$ for a given initial feasible point. This matrix contains elements whose absolute values are different than one. The simplified attractor-repeller $AR$ semidefinite programming relaxation based on the algorithm proposed in [30] is defined as

$$\min \left( -\log \left[ \det \left( \mathbf{B} \circ \mathbf{X} \right) \right] - \sum_{i \neq j} \log(x_{ij}^2) \right),$$

under the conditions $-1 \leq x_{ij} \leq 1$, $\forall i, j : i \neq j$, and where the relaxing constraints for the element $x_{ij}$ are defined. So, in a given point of the matrix $\bar{\mathbf{X}} = (\bar{x}_{ij})$, and $h_{ij}$ is the displacement variable in $\bar{x}_{ij}$. The stop criterion was when the trust region becomes $\leq 10^{-6}$ or $> 4\Delta_0$, where $\Delta_0$ is an initial trust region radius.

---

**Sequential trust-region algorithm**

**Input:**
    a starting point: $X_0$;
    initial trust region radius: $\Delta_0 = 1$;
    input parameters: $r_1 = 0.2$, $r_2 = 1.5$, $c_1 = 0.2$, $c_2 = 0.95$;
**begin**
    $\Delta \leftarrow \Delta_0$;
    $\bar{X} \leftarrow X_0$;
    **while** stopping criteria is satisfied
        solve $(AR_{trust})$: return $trust_X$ & $(h_{ij}, \forall_i, j, i \neq j)$;
        new candidate point: $x_{ij} = \bar{x}_{ij} + h_{ij}, \forall_i, j, i \neq j$;
        compute $det(x_{ij})$;
        **if** $det(x_{ij}) < r_1$
            $\Delta \leftarrow \Delta \cdot c_1$;
        **else**
            $\bar{X} \leftarrow X$;
        **end**
    **end**
    return $\bar{X}$, $trust_X$, $det(x_{ij})$, $det(\bar{X})$;
**end**

**Adaptative multi-start procedure algorithm**

**Input:**
    data matrix: $B$;
    $\beta = 0.9$;
    $k \leftarrow 1$;
**repeat** for a given number of starting points
    a random starting point $X_0$
    start **Sequential trust-region algorithm** from $X_0$: $return\ \bar{X}$, $det\bar{X}$;
    $br \leftarrow 1$;
    **if** $\bar{X}$ is not integral
        **while** $br \leq$ the prescribed number of local searches;
            **do** steepest ascent for the non-integer elements
                till stopping criteria is satisfied
                $\bar{x}_{ij} \leftarrow \bar{x}_{ij} + \beta \cdot inv\left(B \circ \bar{X}\right)_{ij} \cdot det(B)B_{ij}$;
        **end**
        start **Sequential trust-region algorithm** from $\bar{X}$: $return \bar{X}$, $det(\bar{X})$
        $br \leftarrow br + 1$;
    **end**
    **end**
    **if** $\bar{X} \in \{-1,1\}^n$ & $det(B \circ X) > 0$, **then** $X_k \leftarrow \bar{X}$; $k \leftarrow k + 1$;
    **end**
**end**
$X^* = \min_k \{-log\left[det(B \circ X_k)\right]\}$;

Figure 2: The sequential trust-region algorithm pseudocode (adapted from [30])

Figure 3: The adaptative multi-start procedure algorithm pseudocode (adapted from [30])

The steepest ascent algorithm proposed in [30] allows us to ensure that the absolute value of each off-diagonal element does not exceed one, making the current point feasible. Applying the element-wise steepest ascent method, the current point from the local minimum computed by the sequential trust-region algorithm is moved away.

The second step is the adaptative multi-start approach (Fig. 3) proposed in [30]. This algorithm can find the global minimum by restarting the trust-region algorithm from multiple starting points. The starting point is a random and feasible matrix or a matrix obtained from a local minimum.

In this case, $(\mathbf{B} \circ \widetilde{\mathbf{X}})$ has an eigenvalue considerably close to zero. This condition is necessary to backtrack from the sequential trust-region algorithm to a point within the semidefinite region's interior. The steep ascent method must be applied to the non-integer off-diagonal matrix elements of $\widetilde{\mathbf{X}}$. This process must be performed while keeping the fixed integer elements in place. Finally, the adaptative multi-start procedure algorithm allows for random selection of new starting points. This occurs when the local minimum is an integer, or no improvements are found near the non-integral local minimum.

## 3.3   Inversion Procedure and Analysis

As the mathematical description of the objective function is defined for each wavelet type, we can fit the calculated spectrum to the observed one by minimizing the difference between them as a least-squares estimate according to an optimization criterion combining a local-search optimization algorithm with a multi-start procedure. The amplitude and dominant wavelength in the time domain and the amplitude and peak frequency in the frequency domain can be estimated after applying time windowing to the analyzed data. Indeed, when dealing with field data of any kind, it is necessary to use specific techniques to enhance the data, enabling more complex approaches. For instance, techniques such as denoising, surface-wave suppression [1], or the removal of multiples [2, 8] are commonly employed.

The approach described in [37] outlines a workflow that involves cropping a time window from a seismic trace and then sequentially applying the proposed inversion to any number of
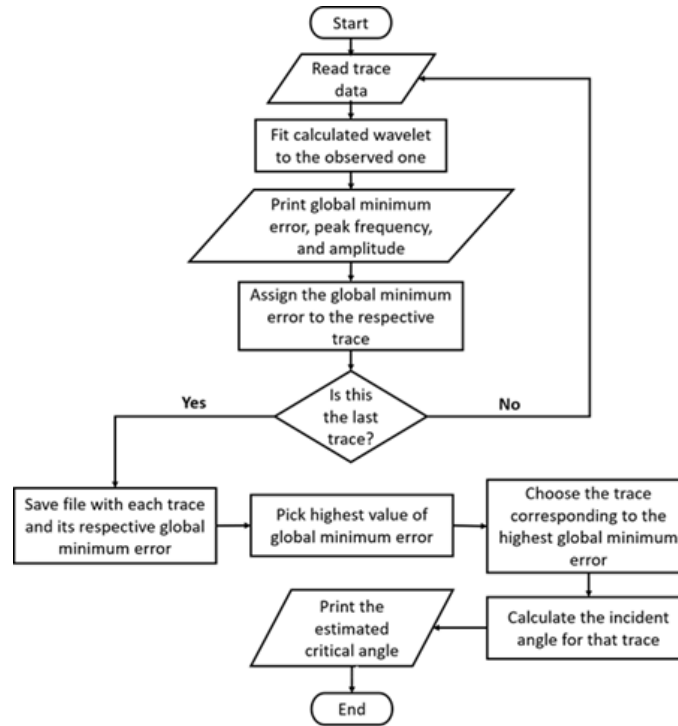
Figure 4: Flowchart of the proposed algorithm (adapted from [37])

traces. As observed in Fig. 4, we adapted this workflow for our implementation.

In Figure 4, note that the block "Fit calculated wavelet to the observed one" is where the inversion procedure described in this and the previous sections is performed. The analysis here focuses on the inversion within the initial sequential loop, as depicted in Fig. 4. Subsequent workflow sequences involve repeated application to other traces, offsets, angles, or time windows. For this reason, we must focus on the inversion procedure employed for the target wavelet since we are interested in knowing how the adapted approach works for different wavelets.

## 4    Results and Discussion

We conducted our tests using the Ricker, Semi-Gaussian, and Gaussian wavelets at $5\,Hz$, $15\,Hz$, $30\,Hz$, $100\,MHz$, and $1\,GHz$ for noise-free and noisy experimental data. These frequencies were selected to cover the range commonly used in geophysical applications. We simulated the wavelets using the finite-difference modeling scheme proposed in [31]. We modeled each pulse with 100 points in time divided by the wavelength. The power was normalized, and the criteria for adding noise employed was applying two of the same wavelets tested with half of the power, e.g., we simulate the addition of two Ricker wavelets with half of the power of the Ricker analyzed.

We compared each wavelet type at each frequency to compute and analyze the error in estimating the signal parameters. This enables us to determine the optimal combination of frequency and wavelet, providing a list of the most suitable geophysical methods for practical use with spectral recomposition approaches. During our experiments, we fitted each wavelet to its respective type. We utilized the multi-start procedure with 100 starting points in each curve fitting. The results of each fitting represent the average minimum value among the 100 inversions. Even though the most important results for being analyzed in these experiments are the residual errors, we added the input and output data scheme in the Appendix to clarify

how the results are obtained.

We observe that the Ricker wavelet performed the best fitting for $5\,Hz$, showing promising results all along the wavelet; see Fig. 5. The Semi-Gaussian and Gaussian wavelets also led to promising results but with slightly higher errors, with the Gaussian wavelet showing a less accurate result than the Semi-Gaussian. In Figure 6, we observe the same accuracy pattern for $15\,Hz$ among the three types of wavelets. However, the error of all of them is increased compared to the results found in Fig. 5. At $30\,Hz$ (Fig. 7), we again observe the same error pattern across all three wavelets but with an increased error level. The results

(a) Noise-free data                                    (b) Noisy data
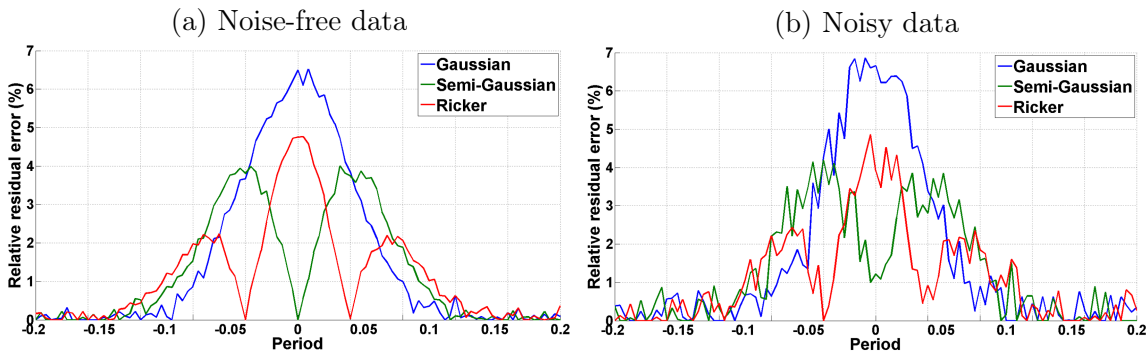


Figure 5: Differences of variations of the normalized residual error along the wavelength related to a frequency of $5\,Hz$ for Ricker, Semi-Gaussian, and Gaussian wavelets
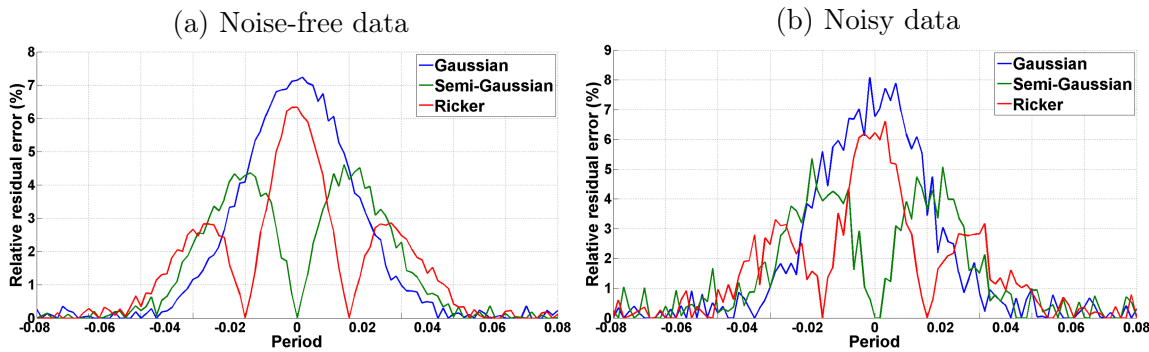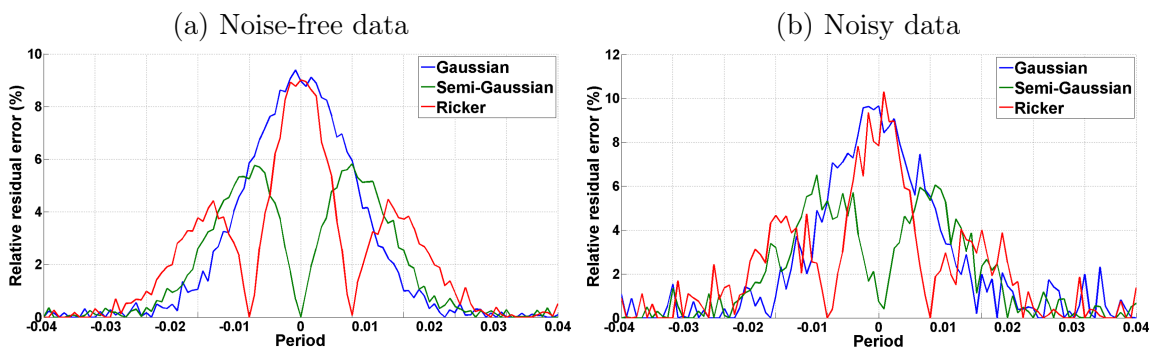
(a) Noise-free data                                    (b) Noisy data



Figure 6: Differences of variations of the normalized residual error along the wavelength related to a frequency of $15\,Hz$ for Ricker, Semi-Gaussian, and Gaussian wavelets
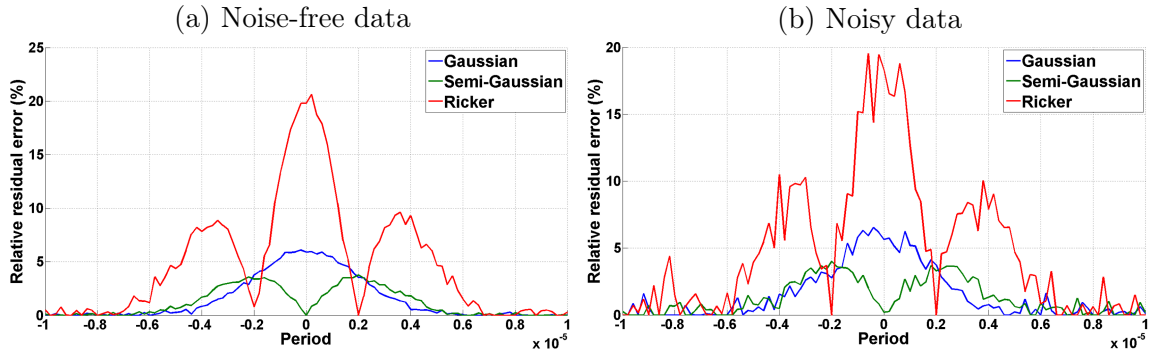
(a) Noise-free data                                    (b) Noisy data



Figure 7: Differences of variations of the normalized residual error along the wavelength related to a frequency of $30\,Hz$ for Ricker, Semi-Gaussian, and Gaussian wavelets
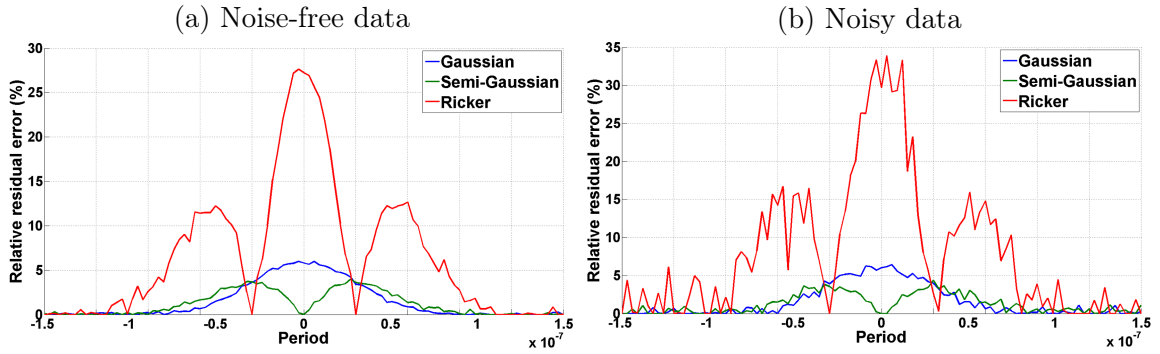
(a) Noise-free data                    (b) Noisy data



Figure 8: Differences of variations of the normalized residual error along the wavelength related to a frequency of $100\,MHz$ for Ricker, Semi-Gaussian, and Gaussian wavelets

(a) Noise-free data                    (b) Noisy data



Figure 9: Differences of variations of the normalized residual error along the wavelength related to a frequency of $1\,GHz$ for Ricker, Semi-Gaussian, and Gaussian wavelets

found in Figs. 5–7 show that the mathematical description of the Ricker wavelet fits very well for lower frequencies ($5\,Hz$, $15\,Hz$, and $30\,Hz$). Since the error found when we fit the Semi-Gaussian wavelet is also low, we can use the mathematical description of Ricker and Semi-Gaussian wavelets for seismic methods. It can be performed by applying the mathematical description of the Ricker wavelet for reflections far from the critical angle. At the same time, we can use the mathematical description of the Semi-Gaussian wavelet to make the reflections closer to the critical angle. The results found for applying the Ricker wavelet are also corroborated by the results obtained in [36, 37, 38]. While these papers have not specifically tested the mathematical description of the Semi-Gaussian wavelet, their observation of significantly higher errors when fitting the Ricker wavelet in Semi-Gaussian wavelets underscores the critical importance of the mathematical description we propose to employ in this study. Another noteworthy finding in these three tested frequencies is that the error in fitting the Ricker wavelet increases along its side lobes with the rising frequency. Note that the higher increase in the relative error for the Ricker wavelet is because its lobes are closer to each other at higher frequencies, making it more challenging to perform an accurate fit.

Figures 8 and 9 illustrate low errors for the Gaussian and Semi-Gaussian wavelets, enabling the application of the mathematical description of the Gaussian wavelet to address petrophysical problems characterized by frequencies on the order of $MHz$. Similarly, the mathematical description of the Semi-Gaussian wavelet facilitates applying this approach for $GPR$ or other electromagnetic methods characterized by frequencies on the order of $GHz$. As discussed in this section, the higher error in fitting the side lobes of Ricker wavelets becomes more

Table 1: Average relative errors for estimating the signal parameters of each frequency and each wavelet with noise-free data

| Frequency | Ricker | Semi-Gaussian | Gaussian |
|---|---|---|---|
| $5\,Hz$ | 2.45% | 3.01% | 3.29% |
| $15\,Hz$ | 3.12% | 3.46% | 3.49% |
| $30\,Hz$ | 4.91% | 5.32% | 5.22% |
| $100\,MHz$ | 12.35% | 2.95% | 3.42% |
| $1\,GHz$ | 18.20% | 2.83% | 3.58% |

Table 2: Average relative errors for estimating the signal parameters of each frequency and each wavelet with noisy data

| Frequency | Ricker | Semi-Gaussian | Gaussian |
|---|---|---|---|
| $5\,Hz$ | 3.34% | 3.95% | 4.34% |
| $15\,Hz$ | 3.98% | 4.57% | 4.41% |
| $30\,Hz$ | 4.72% | 6.86% | 7.00% |
| $100\,MHz$ | 14.71% | 3.98% | 4.59% |
| $1\,GHz$ | 21.07% | 3.82% | 4.73% |

pronounced with increasing frequency. This trend is once more observed at $100\,MHz$ and $1\,GHz$, but with significantly higher errors, underscoring the formidable challenge of employing the Ricker wavelet in this approach. While our approach demonstrated the effectiveness of the Ricker wavelet at $5\,Hz$ (e.g., reflecting events from ultra-deep offshore structures), $15\,Hz$ (e.g., $FWI$), and $30\,Hz$ (e.g., $FWI$ and high-definition seismic techniques), the low-quality results observed at frequencies in the $MHz$ and $GHz$ range limit its application in ultrasound ($MHz$ range) and other methods requiring very high frequencies. The errors in each experiment, related to the objective function, are visible in Tabs. 1 and 2, where we can see that the choice of employed method does not significantly impact the results obtained through spectral recomposition approaches, consistent with the results found in [36, 37]. We also applied our approach to real data. The first case involves a $25\,Hz$ seismic signal (Fig. 10), and the second pertains to a $450\,MHz$ $GPR$ signal (Fig. 11). The experiment involving real seismic data, whose wavelet resembles a Semi-Gaussian with a peak frequency of $25\,Hz$ (Fig. 10), revealed some challenges when performing the curve fitting at lower frequencies. Figures 10(a) and 11(a) are the real data traces analyzed, while Figs. 10(b) and 11(b) are the residual errors from this analysis. However, our approach successfully achieved a low average error when performing this task. Similarly, our approach provided a low average error for estimating the parameters of the $450\,MHz$ $GPR$ signal (Fig. 11). In the real cases, we observed relatively low errors, with low errors along most of the wavelets. However, there were exceptions at the wavelet peaks, where error concentrations were higher for amplitude estimates. This substantial evidence aligns with the results from our synthetic data experiments, demonstrating the practicality of our approach in estimating signal parameters for these real data types. Consequently, our approach was able to accurately estimate peak frequency and phase for all types of wavelets tested in our experiments.

We also performed a test using our approach on the reflection events of a field dataset. This data was recorded near Rotterdam, The Netherlands; see [8] for more details. The data were recorded along a 2D line with an $S$-wave source and horizontal-component receivers oriented in the crossline direction. The data were processed to suppress the surface waves and the free-surface multiples [8]. Figure 12(a) shows the common-source gather ($CSG$), while Fig. 12(b) illustrates how our approach could fit this $CSG$. Figure 12 shows that, despite the difficulty in estimating the phase, our approach can fit accurately concerning the amplitude and frequency.
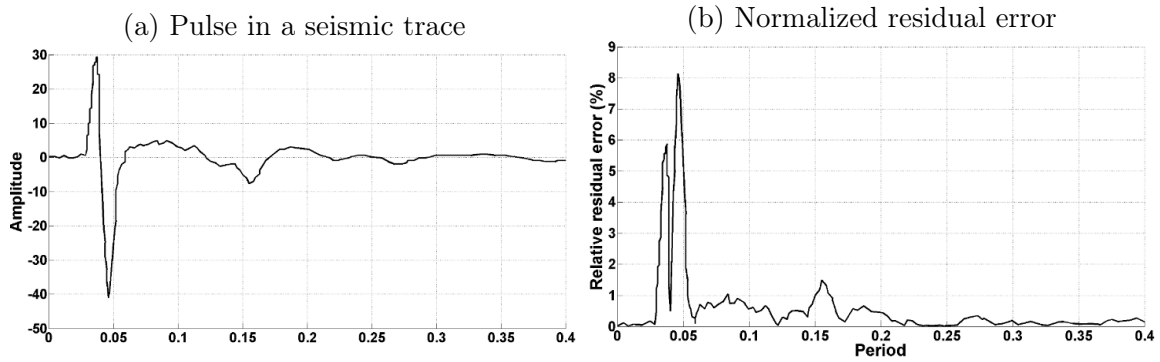
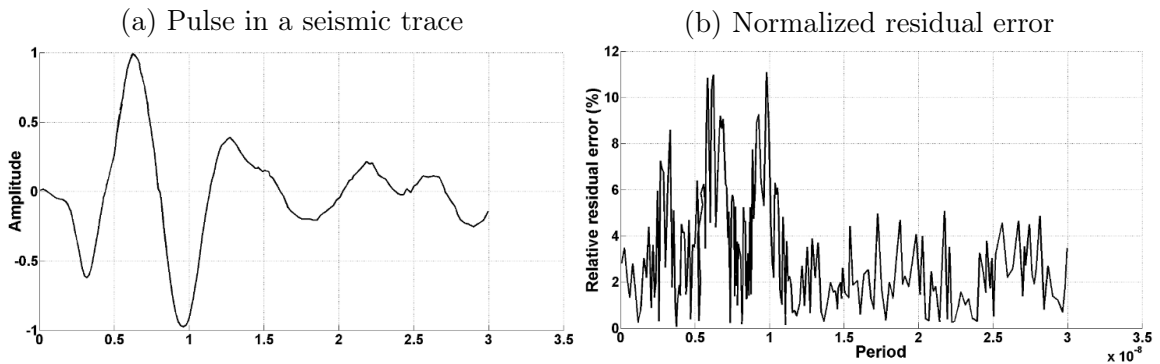Figure 10: Estimating the wavelet with the proposed approach, peak frequency is around $25\,Hz$



Figure 11: Estimating the wavelet with the proposed approach, peak frequency is around $450\,Hz$
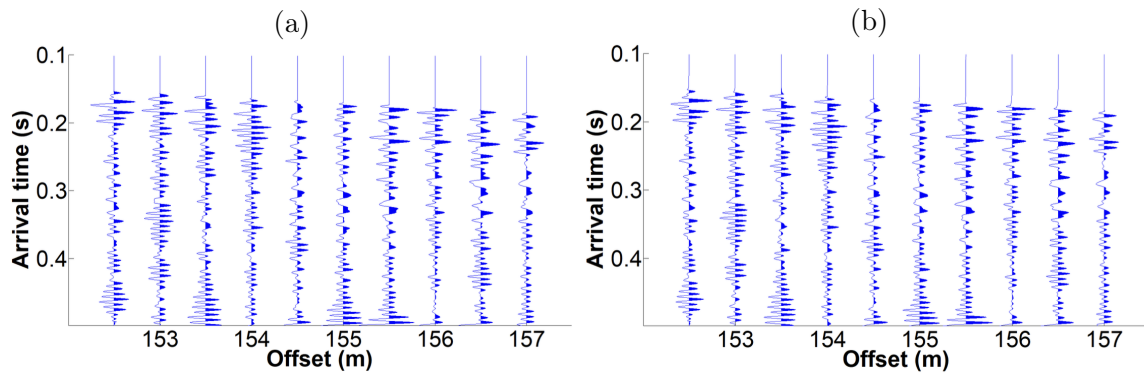


Figure 12: Testing our approach using 2D field dataset, (a) – Original common-source gather, (b) – Common-source gather fitted using our approach.

## 4    Conclusions

We have proposed an alternative implementation and application for an approach that estimates signal properties of a seismic spectrum by reconstructing it in the frequency domain. In our implementation, we adapt the approach to recover the signal properties of three wavelets in the time domain, fitting the calculated wavelet to the observed one. Our proposed approach provides a data-driven manner for performing the spectral analysis, which is significantly faster

than other conventional approaches that demand certain pre-processing. However, since our approach is based on the mathematical description of a wavelet, its employment is required to be performed on a proper wavelet.

To evaluate the capability of our implementation, we have tested it on numerically modeled data of three wavelets (Ricker, Semi-Gaussian, and Gaussian) across different frequency ranges. We have examined our application on synthetic data, allowing us to systematically compare errors without the influence of external factors or peculiarities associated with each method. Our approach has determined which wavelet works better within specific frequency ranges for this type of inversion procedure in the time domain. We have also conducted experiments with real data, and the results have corroborated those obtained from the experiments conducted with synthetic data. Our implementation in the time domain has shown promising results in estimating signal parameters when applied to lower frequency ranges with the Ricker wavelet, reinforcing the results obtained in the frequency domain.

Furthermore, we have observed that our application on lower frequencies with Semi-Gaussian wavelets also yields low errors in estimating signal parameters. This demonstrates that our implementation can be applied effectively for estimating signal parameters in seismic reflection and critical refractions, even in the presence of strong phase shifts. Estimating signal parameters for a high-frequency Semi-Gaussian wavelet ($\sim 1\,GHz$) resulted in low errors, suggesting an effective means of estimating these parameters in $GPR$ pulses. For the Gaussian wavelet with a frequency in the order of $MHz$, we have found that it provides a reliable method for estimating signal parameters with low errors, indicating an interesting application for signal parameter estimation in petrophysics.

Moreover, when estimating the signal parameters of Gaussian wavelets with frequencies in the order of $GHz$, we observed low errors, enabling the application of our approach to estimate signal parameters in the propagation of heat flow. The high errors observed for the Ricker wavelet at higher frequencies indicate that this approach is not recommended for ultrasound applications. Our approach demonstrates the capability to accurately estimate signal parameters, especially the peak frequency and phase, for various wavelets commonly encountered in geophysical surveys.

## Acknowlegements

## Appendix

We provide an additional visual representation to enhance understanding of the methodologies employed, as shown in Fig. 13. This flowchart offers a more visible and intuitive depiction of applying these approaches, using trace data as an example.
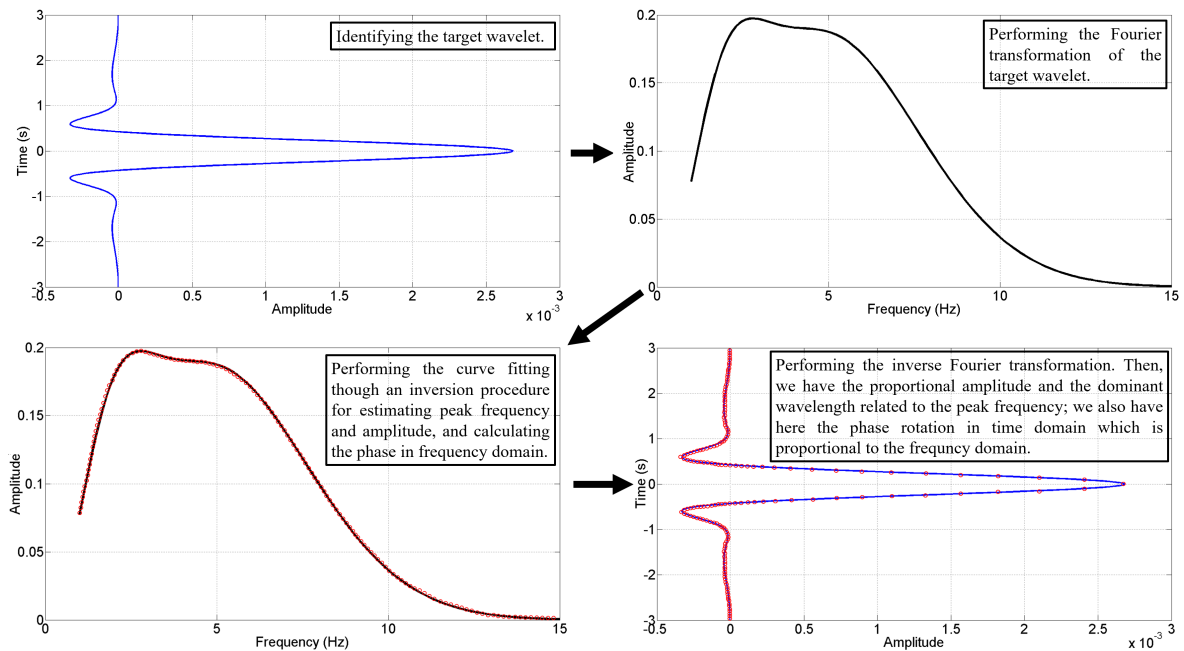
Figure 13: Illustration in the case of time-frequency domain transformation

# References

[1] Balestrini F., Draganov D., Malehmir A., and Ghose R., *Improved target illumination at Ludvika mines of Sweden through seismic-interferometric noise reduction.* Geophysical Prospecting, 68 (2020), 200-213.

[2] Berkhout A., Verschuur D., Wapenaar C., *Adaptive surface-related multiple elimination.* Geophysics, 57.9 (1992), 1166-1177.

[3] Cai Y., Fomel S., Zeng H., *Automated spectral recomposition with application in stratigraphic interpretation.* Interpretation, 1.1 (2013), SA109-SA116.

[4] Castagna J., Sun S., Siegfried R., *Instantaneous spectral analysis: detection of low-frequency shadows associated with hydrocarbons.* Leading Edge, 22 (2003), 120-127.

[5] Dunne J., Beresford G., *A review of the $\tau - p$ transform, its implementation and its applications in seismic processing.* Exploration Geophysics, 26.1 (1995), 19-36.

[6] Fomel S., *Seismic data decomposition into spectral components using regularized nonstationary autoregression.* Geophysics, 78.6 (2013), O69-O76.

[7] Gammaldi S., Ismail A., and Zollo A. *Fluid Accumulation Zone Inferred by Seismic Attributes and Amplitude Versus Offset Analysis at the Solfatara Volcano, Campi Flegrei, Italy.* Front. Earth Sci., 10 (2022), 866534.

[8] Ghose R., Goudswaard J., *Integrating s-wave seismic-reflection data and cone penetration test data using a multiangle multiscale approach.* Geophysics, 69 (2004), 440-459.

[9] Graps A., *An introduction to wavelets.* IEEE Computational Science and Engineering, 2.2 (1995), 50-61.

[10] Hosken J. *Ricker wavelets in their various guises.* First Break, 6.1 (1988), 24-33.

[11] Huang N., Shen Z., Long S., Wu M, Shin H., Zheng Q., Yen N.-C., Tung C., and Liu H., *The empirical mode decomposition and the Hilbert spectrum for nonlinear and non-stationary time series analysis.* Proceedings of the Royal Society A, 454(1971) (1988).

[12] Ismail A., Ewida H.F., Al-Ibiary M.G., and Zollo A., *Integrated prediction of deep-water gas channels using seismic coloured inversion and spectral decomposition attribute, West offshore,*

*Nile Delta, Egypt.* NRIAG Journal of Astronomy and Geophysics, 9.1 (2020), 459-470. DOI: 10.1080/20909977.2020.1768324

[13] Ismail A., Ewida H.F., Al-Ibiary M.G., Nazeri S., Salama N.S., Gammaldi S., and Zollo A., *The detection of deep seafloor pockmarks, gas chimneys, and associated features with seafloor seeps using seismic attributes in the West offshore Nile Delta, Egypt.* Exploration Geophysics, 52.10 (2020), 388-408. DOI: 10.1080/08123985.2020.1827229

[14] Ismail A., Ewida H.F., Nazeri S., Al-Ibiary M.G., and Zollo A., *Gas channels and chimneys prediction using artificial neural networks and multi-seismic attributes, offshore West Nile Delta, Egypt.* Journal of Petroleum Science and Engineering, (2022), 109349. DOI: 10.1016/j.petrol.2021.109349

[15] Javadi M., Ghasemzadeh H., *Wavelet analysis for ground penetrating radar applications: a case study.* Journal of Geophysics and Engineering, 14 (2017), 1189-1202.

[16] Landro M., Tsvankin I., *Seismic critical-angle reflectometry: a method to characterize azimuthal anisotropy?.* Geophysics, 73.2 (2007), D41-D50.

[17] Li Y., Zheng X., Zhang Y., *High-frequency anomalies in carbonate reservoir characterization using spectral decomposition.* Geophysics, 76 (2011), V47-V57.

[18] Li Y., Yang X., Lan T., Liu R., and Qu X., *Parameter inversion by a modified reflected signal reconstruction method for thin-layered media.* IEEE Antennas and Wireless Propagation Letters, 21.5 (2022), 958-962.

[19] Liu Q., Ma J., *Wavelet-based analysis for geophysical data: applications in electromagnetic exploration.* Elsevier, 2006.

[20] Mallat S., *A theory for multiresolution signal decomposition: the wavelet representation.* IEEE Transactions on Pattern Analysis and Machine Intelligence, 11.7 (1998), 674-693.

[21] Mallat S., *A wavelet tour of signal processing: the sparse way.* Academic Press, 1999.

[22] Mitrofanov G., Priimenko V., *Prony filtration of seismic data: theoretical background.* Revista Brasileira de Geofísica, 29.4 (2011), 703-722.

[23] Mitrofanov G., Priimenko V., *Prony filtering of seismic data: mathematical and physical modelling.* Revista Brasileira de Geofísica, 31.1 (2013), 151-168.

[24] Mitrofanov G., Priimenko V., *Prony filtering of seismic data.* Acta Geophysica, 63.3 (2015), 652-678.

[25] Percival D., Walden A., *Wavelet methods for time series analysis.* Cambridge University Press, 2000.

[26] Qu J., Thurber C., *Wavelet-based detection and extraction of fault-related transient waves in seismic data.* Geophysical Journal International, 171.2 (2007), 640-656.

[27] Ren X., Yin C., *Application of wavelet transform in geophysical data processing.* In: IEEE International Geoscience and Remote Sensing Symposium (IGARSS), Held 25-30 July 2010, Honolulu, Hawaii, USA, 1506-1509.

[28] Ricker N., *The form and laws of propagation of seismic wavelets.* Geophysics, 18 (1953), 10-40.

[29] Sil S., Sen M., *Seismic critical-angle anisotropy analysis in the $\tau - p$ domain.* Geophysics, 74.4 (2009), A53-A57.

[30] Terlaky T., Sotirov R., *Multi-start approach to global conic optimization.* ISE Archives of Working Papers, 2010.

[31] Thorbecke J., Draganov D., *Finite-difference modeling experiments for seismic interferometry.* Geophysics, 76 (2011), H1-H18.

[32] Tomasso M,, Bouroullec R., Pyles D., *The use of spectral recomposition in tailored forward seismic modeling of outcrop analogs.* AAPG Bulletin, 94.4 (2010), 457-474.

[33] Wang Y., *Generalized seismic wavelets.* Geophysical Journal International, 203.2 (2015), 1172-1178.

[34] Yan Y., Cui Y., Huang X., Zhou J., Zhang W., Yin S., and Hu S., *Combining seismic signal dynamic inversion and numerical modeling improves landslide process reconstruction.* Earth Surface Dynamics, 10.6 (2022), 1233-1252.

[35] Yan, Y., Chen, X., Li, J., Guan, J., Li, Y., and Cui, S., *Multiparameter shallow-seismic waveform inversion based on the Jensen-Shannon divergence.* Geophysical Journal International, 238.1 (2024), 132-155.

[36] Zuniga N., Priimenko V., *Automated travel-time picking using spectral recomposition.* Brazilian Journal of Geophysics, 39.3 (2021), 375-392.

[37] Zuniga N., Draganov D., Ghose R., *Critical angle of reflections and Poisson's ratio from spectral recomposition.* Journal of Applied Geophysics, 215 (2023), 105110.

[38] Zuniga N., Gioria R., Carmo B., *Spectral recomposition for initial velocity models in full-waveform inversion.* Journal of Applied Geophysics, 215 (2023), 105120.

Nelson Ricardo Coelho Flores Zuniga,
Institute of the Sea, Federal University of São Paulo,
Rua Carvalho de Mendonça, 144 - Encruzilhada - CEP: 11.070-100, Santos-SP, Brazil,
Email: `zuniga@unifesp.br`

Viatcheslav Ivanovich Priimenko,
State University of Norte Fluminense Darcy Ribeiro,
Avenue Brennand, 211 - Imboassica - CEP: 27.925-535, Macaé-RJ, Brazil,
Email: `slava@lenep.uenf.br`